A mechano-electro-acoustical model for the cochlea: Response to acoustic stimuli

Sripriya Ramamoorthy[a] and Niranjan V. Deo[b]
Department of Mechanical Engineering, University of Michigan, Ann Arbor, Michigan 48109

Karl Grosh[c]
Department of Mechanical Engineering and Department of Biomedical Engineering, University of Michigan, Ann Arbor, Michigan 48109

(Received 9 July 2006; revised 22 January 2007; accepted 12 February 2007)

A linear, physiologically based, three-dimensional finite element model of the cochlea is developed. The model integrates the electrical, acoustic, and mechanical elements of the cochlea. In particular, the model includes interactions between structures in the organ of Corti (OoC), piezoelectric relations for outer hair cell (OHC) motility, hair bundle (HB) conductance that changes with HB deflection, current flow in the cross section and along the different scalae, and the feed-forward effect. The parameters in the model are based on guinea-pig data as far as possible. The model is vetted using a variety of experimental data on basilar membrane motion and data on voltages and currents in the OoC. Model predictions compare well, qualitatively and quantitatively, with experimental data on basilar membrane frequency response, impulse response, frequency glides, and scala tympani voltage. The close match of the model predictions with experimental data demonstrates the validity of the model for simulating cochlear response to acoustic input and for testing hypotheses of cochlear function. Analysis of the model and its results indicates that OHC somatic motility is capable of powering active amplification in the cochlea. At the same time, the model supports a possible synergistic role for HB motility in cochlear amplification.
 [DOI: 10.1121/1.2713725]

PACS number(s): 43.64.Bt, 43.64.Kc [WPS] Pages: 2758–2773

I. INTRODUCTION

In this paper, we develop a linear, physiologically based, three-dimensional finite element model of the cochlea that explicitly couples the electrical, acoustic, and mechanical elements of the cochlea. The normal function of the cochlea relies on a carefully orchestrated tripartite mechanical, electrical, and acoustical (fluidic) coupling. Acoustic stimulation of the cochlea launches a fluid-structure traveling wave along the basilar membrane (BM) and other cochlear structures (e.g., Ref. 1) and a concomitant electrical response (one manifestation of which is the cochlear microphonic, e.g., Ref. 2), each correlated to the input stimulus. Artificial intracochlear electrical stimulation results in emission from the ear[3] and predictably alters the mechanical response of the BM to input sound.[4] Since the discovery of outer hair cell (OHC) somatic electromotility,[5] these cells have been the focus of investigation as a mediator of electrical-structural interaction and of amplification. There exists a body of evidence supporting this hypothesis. For instance, it has been found that drugs that decrease OHC motility *in vitro* likewise decrease the amplitude of the BM velocity and sharpness of the frequency filtering in response to acoustic stimulus (e.g., Ref. 6). OHC electromotility covers the entire mammalian auditory frequency range extending to at least 70 kHz *in vitro*[7] and up to 100 kHz *in vivo*.[8] The OHC provides both forward transduction, converting mechanical energy to electrical, and reverse transduction, converting electrical energy to mechanical. Forward transduction also occurs in the OHC stereocilia hair bundle (HB) at acoustic frequencies, as their conductance depends on the rotation of the stereocilia,[9] the so-called mechanoelectrical transducer (MET) sensitivity. The cycle-by-cycle conductance changes are paramount to normal cochlear response as they are hypothesized to drive the OHC electromotility. Reverse HB transduction at acoustic frequencies has been hypothesized[10] as a potential amplification mechanism, leading to the possibility of simultaneous high frequency force generation by the stereocilia and the OHC soma. As measurement techniques are improved and more physiological conditions are used, estimates of the time constant of electrically induced motility of the hair bundle are shifting downward to the tenths of millisecond and postulated to be as fast as 50 μs.[11,12] However, there are no data on electromotile force generation from the stereocilia at frequencies greater than a few Kilohertz.[11,13] Such an effect is not yet included in the model developed in this paper. The coupling of two features, OHC somatic electromotility and HB conductance changes, is included.

Although it has been shown that the OHC electromotility is effective *in vivo*,[8] it is not clear how OHCs can provide amplification at high frequencies in the face of the low transmembrane impedance due to its basolateral membrane capacitance. In order to overcome the reduction in motility due to filtering of the OHC transmembrane potential by the ba-

[a]Currently at Bose Corporation.
[b]Electronic mail: ndeo@umich.edu
[c]Electronic mail: grosh@umich.edu

solateral conductance and capacitance, some modelers use an unreasonably large OHC active force[14] or directly compensate for the reduction in OHC active force with frequency.[15] A detailed micromechanically based model is developed in Ref. 16. In that study, the OHC active force is realistic in its magnitude and proportional to OHC hair bundle deflection. However, an additional constant, but still ad hoc, phase factor is added. Lim and Steele[17] develop a purely mechanical model showing that a feed forward model can be used to produce the correct phasing of an active force applied to the BM. However, an analysis of the currents necessary to pass through the active cells is not performed (as the model is purely mechanical) and the levels of the force needed are not provided. In Ref. 18, a realistic OHC active force is employed along with subpartitions [BM, TM, and reticular lamina (RL)] to show nearly 35 dB relative gain between passive and active response. However, the OHC and HB displacement are not explicitly derived from the micromechanics.

We present a method that explicitly models the electrical, fluid, and mechanical domains and their interaction. This key step is circumvented in most other models by using physiologically motivated arguments linking the response of the BM or the stereocilia directly to the force generated by the OHCs. Dimitriadis and Chadwick[19] proposed a fully coupled model, but presented no predictions from it. We present the piezoelectric behavior of the OHC at a more physiological level than has been done previously by explicitly representing the electrical domain and coupling it to the micromechanics. The model matches qualitatively and quantitatively a wide range of measures seen in experiments. Indeed, the purpose of this paper is to illustrate the close match between the experimental results observed at basal locations in the cochlea and the results predicted using the physiologically based mathematical model. Furthermore, we demonstrate robustness of the model predictions to changes in model parameters. The model results show that OHC somatic force generation is quite capable of producing the amplification seen *in vivo*.

II. THE MODEL

The model has been built with an objective to simulate BM response to acoustic signals. With this aim in mind, simplifications were made while creating the cochlear model, in order to focus on the mechanisms involved and to show their interplay. The fundamental components and assumptions can be listed rather readily, but the details of the modeling, naturally, are somewhat involved. In short, the model couples an inviscid, uncoiled, two-duct model for the macroscopic fluid to the BM (see Fig. 1). The locally reacting model of the BM also interacts with a micro-mechanical model of the organ of Corti (OoC) that includes transverse and radial motion of the TM. Viscosity is incorporated through damping of the OoC and the BM. A cable model is used to represent the macroscopic current flow in the scalae. Electromechanical coupling arises from a piezoelectric model for the OHC soma. The AC transducer current through the HBs is driven by the displacement dependent conductance of the HBs which modulates

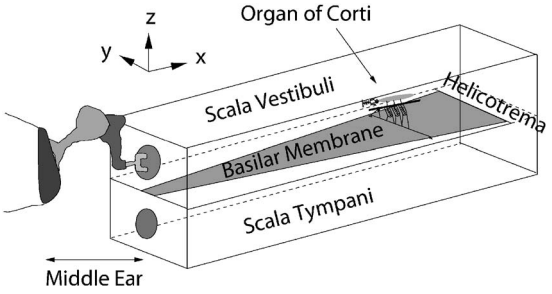

FIG. 1. Illustration of the model used for simulating the cochlea. Organ of Corti is only pictured at one cross section. In the mathematical model it is included over the entire length of the basilar membrane.

the resting potential. We study small perturbations about an operating point. Hence a linearized model is used. These components of the model, their interaction, and the numerical modeling are detailed next.

A. Fluid and the basilar membrane

Figure 1 illustrates a schematic of the standard box model of the cochlea (e.g., Ref. 20) that is used to approximate the fluid domain. The x coordinate is identified with the longitudinal direction of the cochlea, while the y and z coordinates represent a cross section of the cochlea with the z coordinate normal to the BM (the transverse direction), and the y coordinate in the radial direction. The box model for the cochlea is assumed to have rigid walls and is filled with fluid similar to water. The macroscopic fluid response is assumed to be incompressible and nonviscous. For the purpose of this study only harmonic motions of the system were considered. A time dependence of $e^{i\omega t}$ is assumed, where ω is the angular frequency. The governing equation for the (incompressible, inviscid) fluid is

$$\nabla^2 p = 0, \tag{1}$$

where p is the pressure in the fluid. The duct is divided into two equal sections by the BM which lies in the $x-y$ plane. The BM extends to the helicotrema, which is modeled as a 1 mm hole connecting the two ducts. For computational efficiency a modal decomposition of the fluid is used in the radial (y) direction, as in Ref. 20,

$$p(x,y,z) = \sum_{m=0}^{M} p_m(x,z)\cos\left(\frac{m\pi(y+w/2)}{w}\right),$$
$$-\frac{w}{2} \leqslant y \leqslant \frac{w}{2}, \tag{2}$$

where w is the width of the duct, m is the mode number, and M is the total number of modes used in the y direction. The decomposition results in a series of M two-dimensional problems to solve for $p_m(x,z)$. The fluid velocity is related to the fluid pressure by the linearized Euler relation,

$$\nabla p = -i\rho\omega \mathbf{v_f}, \tag{3}$$

where ρ is the density of the fluid (water), and $\mathbf{v_f}$ is the fluid velocity.

The BM is modeled as a set of parallel simply supported beams. Hence, longitudinal stiffness coupling is not included

in the model, as we attribute to the fluid the main coupling in the x direction. Arguments for including longitudinal structural coupling in the BM have been made previously (e.g., Ref. 21). The present model can be extended to include such effects but we have not done so in this paper. The BM motion is decomposed into a sum of modes in the radial direction,

$$u_{\mathrm{bm}}(x,y) = \sum_{n=1}^{N} u_{\mathrm{bm}}^{(n)}(x)\Psi_n(y), \tag{4}$$

where

$$\Psi_n(y) = \sin\left(\frac{n\pi(y+b/2)}{b}\right), \quad -b/2 \leqslant y \leqslant b/2,$$

and b is the width of the membrane. In this study we consider multiple modes for the fluid but only the first mode for the BM. Higher modes of the BM are not included because motion of the BM seen *in vivo* is quite similar to the first symmetric mode.[22] In deriving the equations of motion (Sec. II C) and kinematic relations (Sec. II B 2) only the first mode of the BM is considered. The superscript for the first BM mode has been dropped in subsequent equations in this paper.

Taking advantage of the orthogonality of modes, a series of two-dimensional equations can be obtained for the fluid and the BM by integrating out the radial dependence:

$$\frac{\partial^2 p_m}{\partial x^2} + \frac{\partial^2 p_m}{\partial z^2} - \left(\frac{m\pi}{w}\right)^2 p_m(x,z) = 0, \quad 0 \leqslant m \leqslant M, \tag{5}$$

$$\frac{b}{2}(-M_{\mathrm{bm}}(x)\omega^2 + iC_{\mathrm{bm}}(x)\omega + K_{\mathrm{bm}}(x))u_{\mathrm{bm}}(x) = \sum_{m=1}^{M} (p_m^{\mathrm{SV}} - p_m^{\mathrm{ST}})\mu_m + Q_{\mu\mathrm{mech}}, \tag{6}$$

where M_{bm}, C_{bm}, and K_{bm} are the resultant mass, damping, and stiffness, respectively, for the first structural mode; p_m^{SV} and p_m^{ST} represent the pressure loading on the BM from the fluid corresponding to mode m in the scala vestibuli and scala tympani, respectively; μ_m is the coupling coefficient resulting from the integration of the lateral modes for pressure and BM displacement,[20]

$$\mu_m = \int_{-b/2}^{b/2} \cos\left(\frac{m\pi(y+w/2)}{w}\right)\sin\left(\frac{\pi(y+b/2)}{b}\right)dy, \tag{7}$$

and $Q_{\mu\mathrm{mech}}$ is the force from the micro-electro-mechanical model described in Sec. II C, Eq. (32). The factor $b/2$ in Eq. (6) arises from the integration of the first BM mode over the width of the BM.

B. Micro-electro-mechanical model

1. Electrical environment

The macroscopic spread of current through the different scalae is modeled using one-dimensional cables.[23] Figure 2 shows the circuit at a given cross section in the cochlea. The model includes cables for current flow in the scala vestibuli (SV), the scala tympani (ST), and the scala media (SM). The

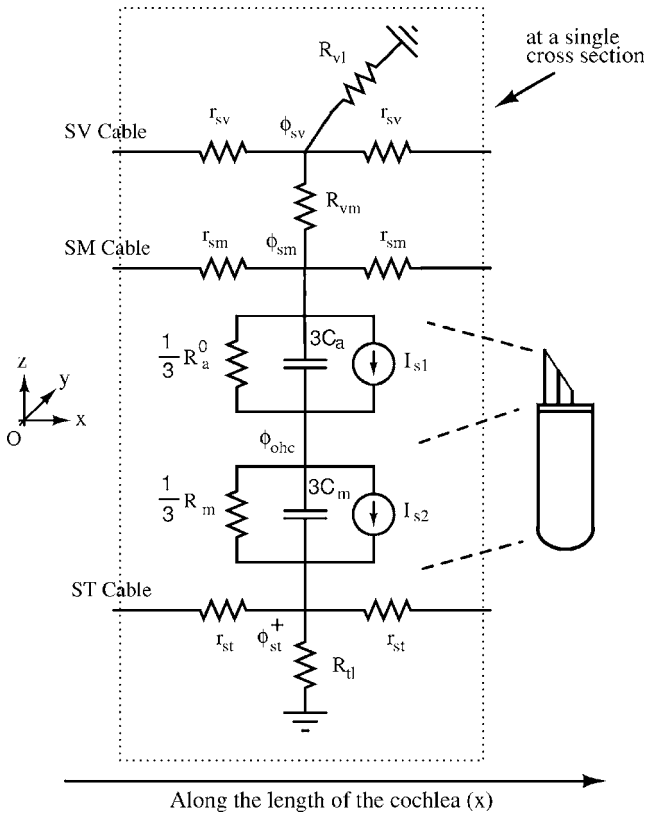

FIG. 2. Electrical network at a given cross section of the cochlea. The SV, SM, and ST cables run longitudinally along the cochlea, ϕ_{st}^{+} represents ST potential at an apical location $(x+\delta x)$ in the cochlea relative to the other quantities. This allows for the possibility of forward inclination of the OHCs (see the feed-forward effect in Sec. II B 4). The factor of three multiplying the apical and the basolateral membrane capacitance, and dividing the apical and the basolateral membrane resistance of the OHC is to account for the three OHCs in a cross section.

ST cable represents the potential in the ST very close to the BM or just in the interstitial space of the OoC, outside the OHCs. Away from the BM, the ST is modeled as being nearly ground. Resistances r_{sv}, r_{sm}, r_{st} represent resistance per unit length along the SV, SM, and ST cables, respectively; R_{vm} is the resistance seen by the current flowing from the SV to the SM; R_{vl} is the resistance to current flowing from SV to ground; R_{tl} is the resistance to flow of current flowing from ST/interstitial space to ground. R_a^0 and C_a represent the apical resistance and capacitance, while R_m and C_m represent the basolateral resistance and capacitance, respectively, of the outer hair cells. I_{s1} and I_{s2} are current sources due to the variable HB conductance and OHC electromotility, respectively [explained in Sec. II B 3, see Eqs. (20) and (23)]. The voltages shown in Fig. 2 represent the fluctuating (or AC) part of voltages in the different scalae. The voltages are at the same cross-section except for the ST voltage. Due to the forward inclination of the OHCs (the feed-forward effect), the ST voltage is located at a certain distance (the feed-forward distance) apical to the location of the other three voltages [see Sec. II B 4, and Eq. (28)].

The electrical domain equations are determined using Kirchhoff's laws. In each cross-sectional circuit branch, there are four electrical potentials, the SV (ϕ_{sv}), the SM (ϕ_{sm}), the OHC (ϕ_{ohc}), and the ST (ϕ_{st}). In addition to cur-

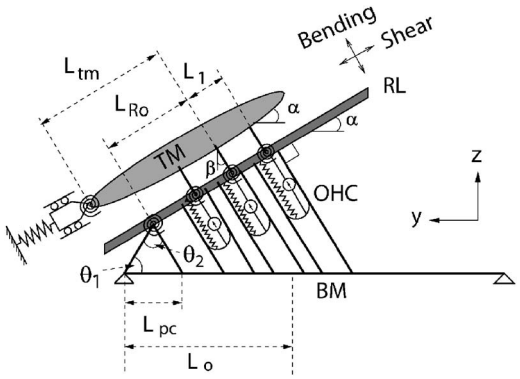

FIG. 3. Micromechanical model for the organ of Corti structures. The sketch is drawn for $\alpha=\beta$ and is pictured here with no feed-forward in the x direction. BM: Basilar membrane; TM: Tectorial membrane; OHC: Outer hair cell; RL-Reticular Lamina. L_{Ro} is the distance between RL pivot point on the arch of Corti and the middle OHC; L_1 is the radial distance between OHCs along the RL; θ_1 is the acute angle between the inner pillar cell and the BM, θ_2 is the acute angle between the inner and outer pillar cell, L_{pc} is the distance along the BM between the left edge of the BM and the contact point of the outer pillar cell with the BM, L_{o} is the distance along the BM between the left edge of the BM and the contact point of the middle OHC with the BM, and L_{tm} is the length of the TM from its pivot to the attachment point of the middle row HBs with the TM.

rent flow in the cross section, current flow along the length of the cochlea is also allowed in the three scalae. Applying Kirchhoff's laws (in both longitudinal and cross-sectional dimensions) to the circuit shown in Fig. 2 yields

$$\frac{1}{r_{\mathrm{sv}}}\frac{\partial^2\phi_{\mathrm{sv}}}{\partial x^2}-\left(\frac{1}{R_{\mathrm{vl}}}+\frac{1}{R_{\mathrm{vm}}}\right)\phi_{\mathrm{sv}}+\frac{1}{R_{\mathrm{vm}}}\phi_{\mathrm{sm}}=0, \tag{8}$$

$$\frac{1}{R_{\mathrm{vm}}}\phi_{\mathrm{sv}}+\frac{1}{r_{\mathrm{sm}}}\frac{\partial^2\phi_{\mathrm{sm}}}{\partial x^2}-\left(\frac{1}{R_{\mathrm{vm}}}+3Y_a\right)\phi_{\mathrm{sm}}+3Y_a\phi_{\mathrm{ohc}}-I_{s1}=0, \tag{9}$$

$$3Y_a\phi_{\mathrm{sm}}-3(Y_a+Y_m)\phi_{\mathrm{ohc}}+3Y_m\phi_{\mathrm{st}}^{+}+I_{s1}-I_{s2}=0, \tag{10}$$

$$3Y_m\phi_{\mathrm{ohc}}+\frac{1}{r_{\mathrm{st}}}\frac{\partial^2\phi_{\mathrm{st}}^{+}}{\partial x^2}-\left(\frac{1}{R_{\mathrm{tl}}}+3Y_m\right)\phi_{\mathrm{st}}^{+}+I_{s2}=0. \tag{11}$$

In Eqs. (8)–(11), $Y_a=1/R_a^0+i\omega C_a=G_a^0+i\omega C_a$ and $Y_m=1/R_m+i\omega C_m$ are the admittances of the apical and basolateral portions of the OHC, respectively. The + superscript indicates a location apical to the longitudinal location under consideration as explained in the section on feed-forward (Sec. II B 4). In this model, the only current path from the SM to the ST is assumed to exist at the apical pole of the OHC and all other junctions at this interface are assumed to be tight.

2. Kinematic model of microstructures

Figure 3 shows a representation of the kinematic model of the (OoC) used in the model. A kinematic model is constructed based on Ref. 24 with different stiffnesses being represented as springs at various locations. The masses of the organ of Corti structures are lumped onto the TM and the BM. The TM is assumed to have two degrees of freedom—a radial (or shear) mode and a transverse (or bending) mode (see Fig. 3). Damping in the system is accounted for through structural damping of the BM and the viscous damping associated with TM motion. Coupling arising from phalangeal processes is neglected, but the feed-forward effect arising from OHC inclination is included. Since the Deiters cell (DC) impedance is in series with OHC impedance and is at least a couple of orders higher in magnitude,[21] the DC is taken as a rigid connection. The RL is modeled as a massless rigid bar. The HBs are also modeled as rigid links. Note that in this representation, the RL and TM are not constrained to stay parallel and the fluid in the sub-tectorial space is not modeled explicitly. The effects of the pressure and fluid motion associated with squeezing the subtectorial fluid layer are not yet included in this model. Only the BM interacts directly with the fluid.

The equations of motion for the OoC are expressed in terms of the BM and the two TM degrees of freedom using Lagrange's method (see Sec. II C). In deriving the equations of motion, the displacement of the OHCs, and the rotation of the HBs and the RL are required. In this section, we list the kinematic assumptions used to express motion of the OHC, HB, and RL in terms of the BM and the TM motion. The kinematic equations obtained in the following are for very small motions. The OHC and HB angles (α and β, respectively) referred to in Fig. 3 pertain to only the middle row OHCs and HBs. Kinematic relations for the middle row OHCs and HBs are first derived ignoring the rigid HB links from the first and third row OHCs (otherwise it is a locked mechanism). The kinematic relations for the first and third row cells are then extrapolated from the middle row relations.

The arch of Corti is assumed to be rigid and hence rotates when the BM is displaced. The displacement of the apical end of the arch of Corti (top of the pillar cells) is therefore given by

$$u_{\mathrm{ap}}(x)=u_{\mathrm{bm}}(x)\Psi_1(b/2-L_{\mathrm{pc}})\frac{\sin(\theta_1+\theta_2)}{\sin(\theta_2)}, \tag{12}$$

where $u_{\mathrm{bm}}(x)$ is the amplitude of the first mode of BM displacement at location x and $\Psi_1(b/2-L_{\mathrm{pc}})$ is the first mode shape of the BM evaluated at $y=b/2-L_{\mathrm{pc}}$ (b is the width of the BM). To determine OHC compression, deflections of the OHC-apex and OHC-base along the OHC are computed. The motion of the middle row OHC-apex toward the BM and along the OHC is given by

$$u_{\mathrm{ohc}_2}^{a}(x)=u_{\mathrm{bm}}(x)\Psi_1(b/2-L_{\mathrm{pc}})\frac{\sin(\theta_1+\theta_2)}{\sin(\theta_2)}\times\left(-\cos(\theta_1-\alpha)+\frac{\cos(\theta_1-\beta)}{\cos(\alpha-\beta)}\right)-u_{\mathrm{tms}}(x)\tan(\alpha-\beta)-u_{\mathrm{tmb}}(x). \tag{13}$$

The motion of the middle row OHC-base toward the RL and along the OHC is

$$u_{\mathrm{ohc}_2}^{b}(x)=u_{\mathrm{bm}}(x)\Psi_1(b/2-L_o)\cos(\alpha). \tag{14}$$

The total compression of the OHC will be the sum of these displacements. However when feed-forward is present, the apical end displacement and basal end displacement of the

OHC will occur at different longitudinal (x) locations. The details of computing the OHC deformation associated with a feed-forward model are discussed in Sec. II B 4.

The twist in the coil spring attached to the HBs is a sum of the rotation of the HBs (due to BM and TM motion) and rotation of the RL (due to BM motion). For small motions, the relative shear motion between the top end (the end connected to the TM) of the middle row HB and its bottom end (connected to the RL), in a direction normal to the HB and toward the outer rows of HBs (toward negative y direction in Fig. 3) is

$$u_{\mathrm{hb}_2}(x) = u_{\mathrm{bm}}(x)\Psi_1(b/2 - L_{\mathrm{pc}})\frac{\sin(\theta_1+\theta_2)}{\sin(\theta_2)}\frac{\sin(\theta_1-\alpha)}{\cos(\alpha-\beta)} + \frac{u_{\mathrm{tms}}(x)}{\cos(\alpha-\beta)}. \tag{15}$$

This HB shear divided by the height of the HB yields the HB rotation relative to its resting position. For small motions, the RL displacement at the location of the middle OHC relative to its (the RLs) attachment at the pillar cells, in a direction normal to itself (RL) and away from the OHC (toward positive z direction in Fig. 3) is given by

$$u_{\mathrm{rl}_2}(x) = -u_{\mathrm{bm}}(x)\Psi_1(b/2 - L_{\mathrm{pc}})\frac{\sin(\theta_1+\theta_2)}{\sin(\theta_2)}\frac{\cos(\theta_1-\beta)}{\cos(\alpha-\beta)} + u_{\mathrm{tms}}(x)\tan(\alpha-\beta) + u_{\mathrm{tmb}}(x). \tag{16}$$

This RL motion at the middle OHC normal to itself divided by distance from the pivot (L_{ro} for the middle OHC) gives the rotation of the RL relative to its resting position. The sum of the HB rotation and RL rotation yields the angle of twist in the coil spring connecting the HBs to the RL.

These quantities can then be derived for the first and third row OHCs and HBs using the middle row displacements as reference and the relative lever ratios. For example, the displacement of the apical end of the first row OHC can be written as

$$u^a_{\mathrm{ohc}_1}(x) = u_{\mathrm{bm}}(x)\Psi_1(b/2 - L_{\mathrm{pc}})\frac{\sin(\theta_1+\theta_2)}{\sin(\theta_2)} \times\left(-\cos(\theta_1-\alpha) + \left[1 - \frac{L_1}{L_{\mathrm{Ro}}}\right]\frac{\cos(\theta_1-\beta)}{\cos(\alpha-\beta)}\right) - \left(1 - \frac{L_1}{L_{\mathrm{Ro}}}\right)u_{\mathrm{tmb}}(x) - \left(1 - \frac{L_1}{L_{\mathrm{Ro}}}\right) \times u_{\mathrm{tms}}(x)\tan(\alpha-\beta). \tag{17}$$

These corrections for the first and third row locations are small and can be neglected. They were however included for the results presented in this paper.

3. Hair bundle conductance and OHC electromotility

The coupling between the electrical domain and the mechanical domain occurs through the variable conductance of the HBs and electromotility of the OHCs. The HBs are assumed to have a conductance which changes linearly with the deflection of the HB,

$$G_{a_j} = G^0_a + G^1_a u_{hb_j}. \tag{18}$$

Here G_{a_j} is the conductance of the jth HB as a function of its deflection u_{hb_j}, where $j=1,2,3$ is the radial counting index for the OHC. G^0_a represents conductance at the resting state ($G^0_a = 1/R^0_a$) of the HB and G^1_a represents slope of the change of conductance with respect to the HB deflection; we will denote this as the mechanoelectrical transducer (MET) sensitivity. G^0_a and G^1_a are assumed constant at a given cross section. The current flowing through the jth HB (I_{hb_j}) is the product of the apical admittance and the potential drop from the SM to the OHC interior. The linearized expression for this current is

$$I_{\mathrm{hb}_j} = (G^0_a + i\omega C_a)(\phi_{\mathrm{sm}} - \phi_{\mathrm{ohc}}) + (V_{\mathrm{sm}} - V_{\mathrm{ohc}})G^1_a u_{\mathrm{hb}_j}, \tag{19}$$

where V_{sm} and V_{ohc} are the voltages at resting state in the SM and the OHC, respectively, and C_a is the apical capacitance of the OHC. As explained in Sec. II B 1, the quantities ϕ_{sm} and ϕ_{ohc} are the fluctuating parts of the voltages in the SM and the OHC, respectively, and are assumed to be the same for each HB at a given cross section. The contribution of the variable conductance to the total HB current at a given cross section is expressed as an equivalent current source I_{s1} in the model (see Fig. 2) whose value is given by

$$I_{s1} = (V_{\mathrm{sm}} - V_{\mathrm{ohc}})G^1_a \sum_{j=1}^{3} u_{hb_j}. \tag{20}$$

The OHC electromotility is modeled through linearized expressions relating OHC strain and transmembrane voltage to the OHC force and current[25] as

$$F_{\mathrm{ohc}_j} = K_{\mathrm{ohc}} u^{\mathrm{comp}}_{\mathrm{ohc}_j} + \epsilon_3(\phi_{\mathrm{ohc}} - \phi^+_{\mathrm{st}}), \tag{21}$$

$$I_{\mathrm{ohc}_j} = (\phi_{\mathrm{ohc}} - \phi^+_{\mathrm{st}})/Z_m - i\omega\epsilon_3 u^{\mathrm{comp}}_{\mathrm{ohc}_j}. \tag{22}$$

Here F_{ohc_j} is the force exerted by the jth OHC on the BM and the RL, I_{ohc_j} is the current flowing through the jth OHC, $u^{\mathrm{comp}}_{\mathrm{ohc}_j}$ represents compression in the jth OHC, ϵ_3 is the electromechanical coupling coefficient, Z_m is the net basolateral impedance of the OHC given by $1/Z_m = 1/R_m + i\omega C_m$ (see Fig. 2), $(\phi_{\mathrm{ohc}} - \phi^+_{\mathrm{st}})$ is the alternating (AC) basolateral transmembrane potential (the term ϕ^+_{st} is explained in Sec. II B 4, and K_{ohc} is the stiffness of the OHC. The potentials and OHC properties ($K_{\mathrm{ohc}}, \epsilon_3, Z_m$) are assumed to be the same for each OHC at a given cross section. The current source I_{s2} shown in Fig. 2 corresponds to the total current due to the piezoelectric-like behavior of the OHC,

$$I_{s2} = -i\omega\epsilon_3 \sum_{j=1}^{3} u^{\mathrm{comp}}_{\mathrm{ohc}_j}. \tag{23}$$

Equations (19) and (22) show how deformation of the organ of Corti leads to additional current flow through the

HBs and the OHCs, while Eq. (21) shows how modulation of the OHC transmembrane potential leads to an equivalent force generation by the OHCs.

4. Feed-forward

The OHCs *in vivo* are inclined toward the base of the cochlea. This inclination is hypothesized to "feed-forward" the energy[26] in the cochlea. Therefore, the force exerted by an OHC is not completely in the $y-z$ plane. To include the feed-forward effect, we now have to decompose F_{ohc_j} into apical and basal locations.

$F^a_{\mathrm{ohc}_j}$ represents force at the apical end (or top end) of the jth OHC. Similarly $F^b_{\mathrm{ohc}_j}$ represents force at the basal end (or bottom end) of the jth OHC. $F^a_{\mathrm{ohc}_j}(x)$ depends on field quantities at x and at $x+\delta x$ while $F^b_{\mathrm{ohc}_j}(x)$ depends on field quantities at x and $x-\delta x$, where δx is the feed-forward distance,

$$F^a_{\mathrm{ohc}_j}(x) = (K_{\mathrm{ohc}}(u^a_{\mathrm{ohc}_j} + u^{b+}_{\mathrm{ohc}_j}) + \epsilon_3(\phi_{\mathrm{ohc}} - \phi^+_{\mathrm{st}}))\cos(\psi), \tag{24}$$

$$F^b_{\mathrm{ohc}_j}(x) = (K_{\mathrm{ohc}}(u^{a-}_{\mathrm{ohc}_j} + u^b_{\mathrm{ohc}_j}) + \epsilon_3(\phi^-_{\mathrm{ohc}} - \phi_{\mathrm{st}}))\cos(\psi), \tag{25}$$

where ψ is the angle of forward inclination (toward the base) of the OHCs with the vertical. Expressions for $u^a_{\mathrm{ohc}_j}$ and $u^b_{\mathrm{ohc}_j}$ are given in Eqs. (13) and (14) in Sec. II B 2. The + and − superscripts represent locations apical or basal, respectively, to the given location in the cochlea, i.e., the displacements and voltages at location $x+\delta x$ and $x-\delta x$, respectively, if x is the location under consideration. Since the feed-forward distance is small ($\approx 5-10\ \mu$m), in our implementation we use the Taylor series approach and retain only the first-order terms. That is,

$$u^{b+}_{\mathrm{ohc}_j} = u^b_{\mathrm{ohc}_j}(x+\delta x) = u^b_{\mathrm{ohc}_j}(x) + \frac{du^b_{\mathrm{ohc}_j}(x)}{dx}\delta x, \tag{26}$$

$$u^{a-}_{\mathrm{ohc}_j} = u^a_{\mathrm{ohc}_j}(x-\delta x) = u^a_{\mathrm{ohc}_j}(x) - \frac{du^a_{\mathrm{ohc}_j}(x)}{dx}\delta x, \tag{27}$$

$$\phi^+_{\mathrm{st}} = \phi_{\mathrm{st}}(x+\delta x) = \phi_{\mathrm{st}}(x) + \frac{d\phi_{\mathrm{st}}(x)}{dx}\delta x, \tag{28}$$

$$\phi^-_{\mathrm{ohc}} = \phi_{\mathrm{ohc}}(x-\delta x) = \phi_{\mathrm{ohc}}(x) - \frac{d\phi_{\mathrm{ohc}}(x)}{dx}\delta x. \tag{29}$$

C. Local governing equations

The derivation of the local equations for the mechanical degrees of freedom is described in this section. The dependence of the variables on the axial location x has been assumed and not explicitly written. The kinetic and potential energy for this whole system, at a given location x, can then be written as

$$\mathcal{T} = \frac{1}{2}M_{\mathrm{tms}}\dot{u}^2_{\mathrm{tms}} + \frac{1}{2}M_{\mathrm{tmb}}\dot{u}^2_{\mathrm{tmb}} + \frac{1}{2}M_{\mathrm{bm}}\dot{u}^2_{\mathrm{bm}}, \tag{30}$$

$$\begin{aligned}\mathcal{V} = {} & \frac{1}{2}K_{\mathrm{bm}}u^2_{\mathrm{bm}} + \frac{1}{2}K_{\mathrm{tms}}u^2_{\mathrm{tms}} + \frac{1}{2}K_{\mathrm{tmb}}u^2_{\mathrm{tmb}} + \frac{1}{2}K_{\mathrm{hb}} \\ & \times \left(\left(u_{\mathrm{hb}_1} + u_{\mathrm{rl}_1}\frac{L_{\mathrm{hb}}}{L_{\mathrm{Ro}} - L1}\right)^2 + \left(u_{\mathrm{hb}_2} + u_{\mathrm{rl}_2}\frac{L_{\mathrm{hb}}}{L_{\mathrm{Ro}}}\right)^2 \right. \\ & \left. + \left(u_{\mathrm{hb}_3} + u_{\mathrm{rl}_3}\frac{L_{\mathrm{hb}}}{L_{\mathrm{Ro}} + L_1}\right)^2\right) + \frac{1}{2}K_{\mathrm{rl}}\left(u_{\mathrm{rl}_2} + \frac{u_{\mathrm{ap}}}{L_{\mathrm{po}}}L_{\mathrm{Ro}}\right)^2,\end{aligned} \tag{31}$$

where u_{tms}, K_{tms}, M_{tms} represent the displacement, stiffness, and mass of the TM shear mode, respectively, and u_{tmb}, K_{tmb}, M_{tmb} represent corresponding quantities for the TM bending mode. In Eqs. (30) and (31) the rotational stiffnesses of the coil springs for the HBs, the TM, and the RL are converted to equivalent linear stiffnesses after multiplying with appropriate lengths.

The generalized work done by external forces (including the electromotile forces from the OHCs, the acoustic pressure, and nonconservative viscous damping) is given by

$$\begin{aligned}Q = {} & -\sum_{j=1}^{3} F^a_{\mathrm{ohc}_j}u^a_{\mathrm{ohc}_j} \\ & -\sum_{j=1}^{3} F^b_{\mathrm{ohc}_j}u^b_{\mathrm{ohc}_j} - \sum_m (p^{\mathrm{SV}}_m - p^{\mathrm{ST}}_m)u_{\mathrm{bm}}\mu_m \\ & -(C_{\mathrm{bm}}\dot{u}_{\mathrm{bm}})u_{\mathrm{bm}} - (C_{\mathrm{tms}}\dot{u}_{\mathrm{tms}})u_{\mathrm{tms}} - (C_{\mathrm{tmb}}\dot{u}_{\mathrm{tmb}})u_{\mathrm{tmb}}.\end{aligned} \tag{32}$$

The net normal fluid force acting on the TM from the sulcus and SM is assumed to be smaller than the normal HB forces acting on the TM. Hence, the TM interaction with the fluid is not included. The BM interacts with the fluid through the pressure difference in the SV and ST [see Eq. (6)]. The expression for $F^a_{\mathrm{ohc}_j}$ and $F^b_{\mathrm{ohc}_j}$ can be obtained from Eqs. (24) and (25). The terms C_{bm}, C_{tms}, and C_{tmb} represent viscous damping coefficients for BM, TM bending, and TM shear modes, respectively.

The governing equations of motion for the mechanical variables, including coupling to the electrical and acoustic domains, are found from the variation of the Lagrangian ($L = \mathcal{T} - \mathcal{V}$) with respect to the three mechanical variables (u_{bm}, u_{tms}, and u_{tmb}):

$$\frac{\partial}{\partial t}\frac{\partial L}{\partial \dot{u}_j} - \frac{\partial L}{\partial u_i} = \frac{\partial Q}{\partial u_i}, \tag{33}$$

where i varies over bm, tms, and tmb. The expressions for the final set of equations are not listed due to space constraints.

D. Finite elements

The expressions given in the preceding sections constitute the strong form of the equations. These are used to derive the weak form after multiplying with corresponding weighting functions and integrating over the domain.[20] The final set of equations have the following form:

TABLE I. Geometric data for the macromodel (see Fig. 3).

Property	Value	Source
BM width (b)	80 μm (base) to 200 μm (apex)	Ref. 28
BM thickness (h)	7 μm (base) to 1 μm (apex)	Ref. 28
L_{pc}	$b/3$	Adapted from Refs. 33 and 24
L_1	9 μm	Based on OHC diameter
L_0	$b/2$	Adapted from Refs. 33 and 24
L_{tm}	60 μm (base) to 180 μm (apex)	Adapted from Refs. 33 and 24
L_{Ro}	Calculated from Fig. 3	
α	25° (base) to 45° (apex)	Ref. 34
β	25° (base) to 45° (apex)	Assumed
θ_1	60°	Adapted from Refs. 33 and 24
θ_2	60°	Adapted from Refs. 33 and 24
L_{ohc}	20 μm (base) - 85 μm (apex)	Ref. 34
L_{hb}	1 μm (base) - 6 μm (apex)	Ref. 9
Duct height for SV, ST (H)	1 mm	Ref. 28
Duct width (W)	1 mm	Ref. 28
Duct length (L)	25 mm	Ref. 28

$$\begin{bmatrix} \mathbf{K_f} & \mathbf{Q_{fs}} & \mathbf{0} \\ \mathbf{Q_{sf}} & \mathbf{K_s} & \mathbf{Q_{se}} \\ \mathbf{0} & \mathbf{Q_{es}} & \mathbf{K_e} \end{bmatrix} \begin{pmatrix} \mathbf{p} \\ \mathbf{u} \\ \phi \end{pmatrix} = \begin{pmatrix} \mathbf{f_f} \\ \mathbf{0} \\ \mathbf{0} \end{pmatrix}. \tag{34}$$

The matrix is unsymmetric due to the nonreciprocal MET function ($\mathbf{Q_{es}} \neq \mathbf{Q_{se}^T}$) and the feed-forward effect. Linear spatial interpolations are used for the structural and electrical degrees of freedom while bilinear interpolations are used for the fluid. The quantity $\mathbf{K_f}$ is the dynamic stiffness of the fluid, $\mathbf{K_s}$ is the dynamic stiffness of the micromechanical structures, and $\mathbf{K_e}$ represents the interaction among the electrical degrees of freedom. Among the off-diagonal terms, $\mathbf{Q_{es}}$ and $\mathbf{Q_{se}}$ represent electrical-structural coupling at the OHCs, and $\mathbf{Q_{fs}}$ and $\mathbf{Q_{sf}}$ are from fluid-structure coupling at the BM. On the right-hand side, $\mathbf{f_f}$ represents any forcing on the fluid. Using a reference displacement at the stapes, the linear matrix equation is solved to determine the fluid pressure ($\mathbf{p}$), structural displacements ($\mathbf{u}$), and electrical potentials (ϕ) at the nodes.

III. MODEL PARAMETERS

The model has a necessarily large number of parameters. The values are listed in Tables I–III. Where possible, we used or extrapolated parameters from published data (references indicated in the tables). In this section, we describe how the parameters were selected and the assumptions underlying those data for which hard experimental values are not available.

A. Mechanical parameters

The effective BM stiffness for the first mode is calculated from the radial flexural rigidity estimated in Ref. 27. For a simply supported BM, the radial flexural rigidity (D) is estimated to be about 2.5×10^{-1} N m for basal locations in the guinea pig.[27] Using this value, one can compute the effective BM stiffness for the first mode,

$$K_{bm} = D\left(\frac{\pi}{b}\right)^4, \tag{35}$$

where b is the width of the BM. The BM thickness (h) and width (b) are estimated from Ref. 28. Although variation in D along the length of the BM was not found to be statistically significant,[27] the radial flexural rigidity is expected to depend on the BM thickness h ($D\propto h^3$). We therefore include a cubic dependence of D on the BM thickness h. Accounting for this difference in interpretation of D, and estimating the BM thickness to be 6.6 μm and BM width to be 90 μm at about 1 to 2 mm from the base (corresponding to the location where point stiffness measurements were made by Gummer *et al.*[27]), the estimated K_{bm} for the most basal location ($x=0$) works out to 6.69×10^7 N/m^2. We use a value of 6×10^7 N/m^2 at $x=0$ in the model.

HB stiffness measurements were made in guinea pigs by Strelioff and Flock.[29] Those measurements were extrapolated to indicate average stiffness of HBs ranging from 63.9 to 284 mN/m for different rows of OHCs at the extreme base of the cochlea ($x=0$). To choose a value for the model the following considerations were made. Using a density of 100

TABLE II. Mechanical properties for the macromodel. x is in meters.

Property	Value	Source
BM stiffness (K_{bm})	$6\times10^5(h/h_0)^3(b_0/b)^4$ N/m^3	Ref. 27
TM bending stiffness (K_{tmb})	$6\times10^3e^{(-220x)}$ N/m^2	Ref. 31
TM shear stiffness (K_{tms})	$6\times10^3e^{(-220x)}$ N/m^2	Ref. 31
RL stiffness (K_{rl})	$7.6\times10^3e^{(-325x)}$ N/m^2	Based on Ref. 24
HB stiffness (K_{hb})	$3.42\times10^4e^{(-325x)}$ N/m^2	Estimated from Ref. 29
OHC stiffness (K_{ohc})	$7.6\times10^3e^{(-325x)}$ N/m^2	Ref. 30 (see Sec. III A)
BM mass per unit area (M_{tm})	$\rho_{bm}h$ kg/m^2	Density assumed
	$\rho_{bm}=1000$ kg/m^3	
BM viscous damping (C_{bm}) (includes fluid viscosity)	0.05 N s/m^2	Assumed
TM bending damping (C_{tmb})	0.05 N s/m^2	Assumed
TM shear damping (C_{tms})	0.03 N s/m^2	Assumed
Effective TM shear mass (M_{tms})	$\rho_{tm}h_{tm}^0b_{tm}^0e^{50x}$ kg/m	x variation assumed
	$\rho_{tm}=1000$ kg/m^3, $h_{tm}^0=18$ μm,	
	$b_{tm}^0=60$ μm	
Effective TM bending mass (M_{tmb})	$0.7M_{tms}$ kg/m	Assumed
Round window stiffness	1.8×10^5 N/m^3	Assumed
Round window damping	5.8×10^4 N s/m^3	Assumed

rows of HBs per mm for guinea pigs[9] yields a stiffness ranging from 6.39 to 28.4 kN/m^2 at $x=0$. Strelioff and Flock[29] used a large displacement of 1 μm to measure stiffness of HBs and their measurements were not taken instantaneously at the application of stimulus. A recent study by Kennedy *et al.*[11] has shown that under excitatory stimulation, the HB stiffness noticeably reduces with time. Because of the latter point, at $x=0$ a slightly higher number of 34 kN/m^2 is used as the average stiffness for HBs in the model. Strelioff and Flock[29] further showed that the HB stiffness decreased at an exponential rate from the base. The decay rate for the HB stiffness varied from −238 to −406 m^{-1} between different rows of OHCs. For simplicity a value of −325 m^{-1} for the decay rate is chosen, which is near the middle of the published range.

TABLE III. Electrical properties for the macromodel. x in meters.

Property	Value	Source
ϵ_3	$(-8\times10^{-6}-8\times10^{-5}x)$ N/m/mV	Ref. 38
$1/R_a^0$	100 μS/m	Estimated using Ref. 36
$1/R_m$	5100 μS/m (base) - 360 μS/m (apex)	Ref. 35
C_a	50 nF/m	Estimated using Ref. 36
C_m	1800 nF/m (base) - 4200 nF/m (apex)	Ref. 35
G_a^1	variable (see Sec. III B)	Free parameter
$V_{sm}-V_{ohc}$	(150-1000x) mV	Based on Ref. 37
R_{vl}	10 Ωm	Based on Ref. 37
R_{tl}	4 Ωm	Based on Ref. 37
R_{vm}	25 Ωm	Based on Ref. 37
r_{sv}	3 MΩ/m	Based on Ref. 37
r_{sm}	5 MΩ/m	Based on Ref. 37
r_{st}	0.15 Ω/m	Based on R_{OC} in Ref. 37

OHC stiffness values are available in literature[30]. The stiffness at resting state *in vivo* and its variation along the length of the cochlea are not known exactly. We use a resting stiffness value of about 11 mN/m for OHCs located 6 mm from the base. The value listed in Table II gives OHC stiffness per meter assuming 100 rows of OHCs in 1 mm.[9] The spatial variation of OHC stiffness along the length of the BM is assumed to be same as that of the HB stiffness.

The stiffnesses of other microstructures (TM, RL) are difficult to estimate, in part because the mode of operation (kinetics and kinematics) is still not completely known. In this paper, we put forth a hypothesis of the dominant kinematics that follows closely that proposed by Dallos.[24] We use estimates of the TM stiffness from Zwislocki and Cefaratti[31] as a guide to choose TM bending and shearing stiffness values. The mass of the TM is calculated from dimensions of the TM and using the density of water (1000 kg/m^3). Following Gummer *et al.*,[32] the TM bending mass is chosen to be 30% lower than TM shear mass (results indicate that TM bending resonance is higher than TM shear resonance[32]).

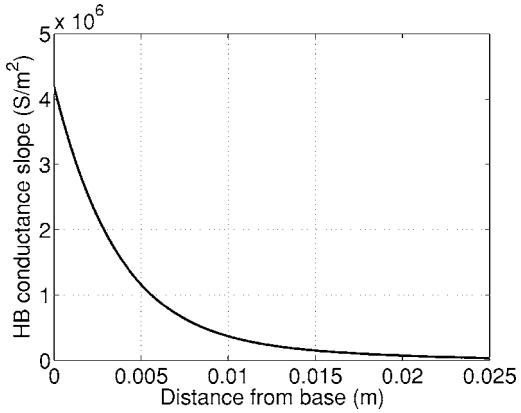

FIG. 4. The plot vs x of the function [Eq. (36)] used for the MET channel sensitivity in the model.

Based on the calculations in Dallos,[24] the value for the RL stiffness [K_{rl}, see Eq. (31)] is chosen to be similar to that of the OHC stiffness. The spatial variation of the RL stiffness is not known and is taken to be the same as that of the HB and OHC stiffness. The viscous modal damping for the three structural degrees of freedom is also not known. In the model, the structural damping is supposed to account for the damping losses associated with the relative motion of the various components of the OoC. The damping chosen for the model is a fit to give reasonable BM passive gain relative to stapes. Dimensions and various angles used are estimated based on Refs. 24 and 28, the OoC sketch shown in Ref. 33, and data from Refs. 9 and 34.

We use a reference displacement at the stapes to solve for the acoustic response. Therefore, only the round window impedance is included in the model, for the rest of the middle ear is not required for the results presented in this study. The round window termination is modeled as a spring and damper interacting with the fluid in the lower duct. The fluid geometry is given in Table I and fluid density is taken as that of water (1000 kg/m^3). As a simplification, we use a uniform cross-section two-duct model with a cross-sectional area corresponding to a basal location in a guinea pig (the extension to a nonuniform area is straightforward, but we have chosen not to study this effect). The fluid model is

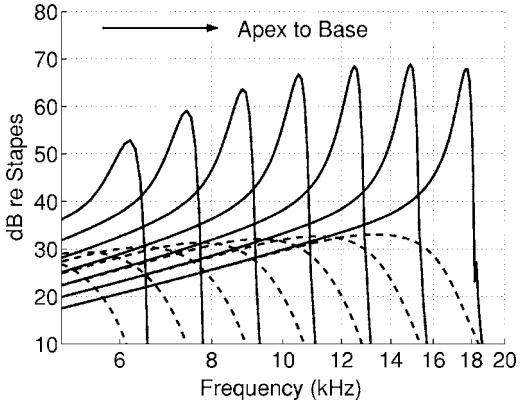

FIG. 5. BM magnitude at different locations in dB normalized to stapes motion (i.e., BM gain relative to stapes). Dash curves: passive ($G_a^1(0)=0$ S/m^2) and solid curves: active ($G_a^1(0)=4.19\times10^6$ S/m^2). Locations are (from left to right). 11.75, 10.75, 9.75, 8.75, 7.75, 6.75, and 5.75 mm.

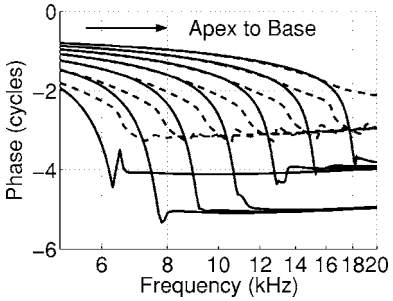

FIG. 6. BM phase at different locations in cycles (2π rad). Dash curves: Passive ($G_a^1(0)=0$ S/m^2) and solid curves: Active ($G_a^1(0)=4.19\times10^6$ S/m^2). Locations are (from left to right) 11.75, 10.75, 9.75, 8.75, 7.75, 6.75, and 5.75 mm.

considered an approximation to the three-dimensional fluid effects. In order to model the true fluid geometry, one would have to build an intricate model of the sulcus and the subtectorial membrane spaces. Such a model would be computationally expensive. Our goal is to build the simplest model that represents the fundamental trends and mechanics of the passive and active response of the cochlea to acoustic stimulation.

B. Electrical parameters

The resistances and capacitances of the apical and basolateral portion of the OHC are known from measurements and model estimates.[35,36] The present model possesses the 1 kHz RC cut-off in OHCs for basal locations. The values shown for these quantities in Table III assume that there are 100 rows of OHCs per millimeter in a guinea pig.[9] The endocochlear potential is taken from Ref. 37. Various resistances in the model are chosen based on Ref. 37 although variation of the resistances along the length is not included. The longitudinal resistance in the scala tympani represents longitudinal resistance in the interstitial space in the OoC. Hence the value of resistance used for that cable is as per the value used in Ref. 37 for the OoC cable resistance. The electro-mechanical coupling coefficient (ϵ_3) along the cochlea is estimated from Ref. 38.

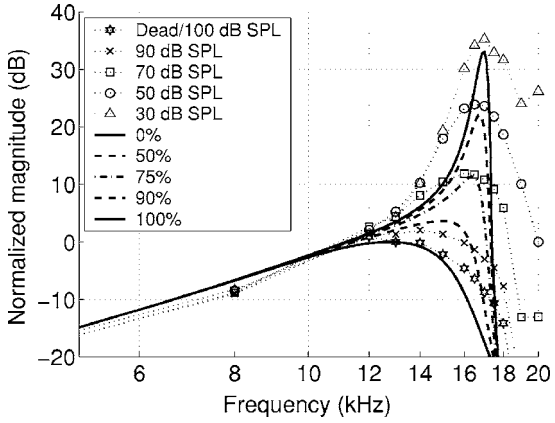

FIG. 7. Dotted lines with markers: Normalized guinea pig data from Cooper (Ref. 39). Thick lines: Theoretical prediction for BM magnitude in decibel at 6 mm for different levels of activity [100% activity is equivalent to a conductance slope of $G_a^1(0)=4.19\times10^6$ S/m^2]. Magnitudes are normalized with respect to maximum passive response.

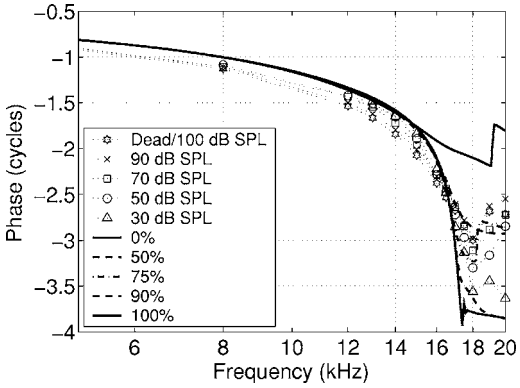

FIG. 8. Dotted lines with markers: Guinea pig data from Cooper (Ref. 39). Thick lines: BM phase in cycles (2π rad) at 6 mm for different levels of activity [100% activity is equivalent to a conductance slope of $G_a^1(0) = 4.19 \times 10^6$ S/m^2].

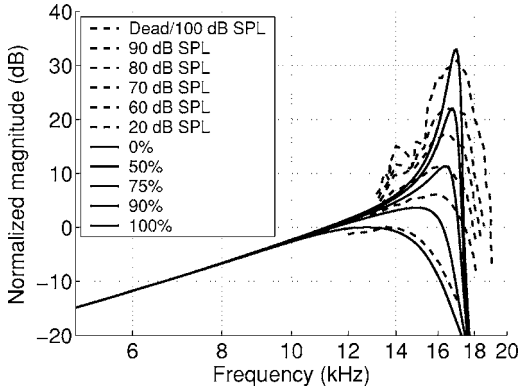

FIG. 9. Dash lines: Normalized guinea pig data from deBoer (Ref. 40); higher gains correspond to lower dB SPLs. Solid lines: Theoretical prediction for BM magnitude in decibels at 6 mm for different levels of activity [100% activity is equivalent to a conductance slope of $G_a^1(0) = 4.19 \times 10^6$ S/m^2]. Higher gains correspond to higher conductance slope. Magnitudes are normalized with respect to maximum passive response.

The MET sensitivity (i.e., the relation between the HB rotation to the change in HB conductance) is kept as a free variable in the model. Having zero MET sensitivity is roughly equivalent to a passive cochlea. Increasing MET sensitivity increases the gain in the model. As expected, the model depends nonlinearly (and strongly) on the MET sensitivity. Indeed, if the MET sensitivity is increased beyond a critical limit, the model response becomes unstable. We found that different regions on the BM have different maximum values of the MET sensitivity such that the global response was stable. A polynomial-exponential dependence was used for the variation of the MET sensitivity in the model,

$$G_a^1(x) = G_a^1(0)(-10^5 x^3 + 5.9 \times 10^3 x^2 - 109x + 1.0)e^{-150x}, \tag{36}$$

where x is in meters. Figure 4 shows the function $G_a^1(x)$ given in Eq. (36) plotted against x. This dependence was found from numerical experimentation and comparison of predictions with experiments. The maximum value for $G_a^1(0)$ at which the response of the model is stable is 4.19×10^6 S/m^2. Our empirically determined spatial variation for the MET channel sensitivity is used throughout the study. The entire spatial pattern for the MET sensitivity is scaled by the multiplying factor $G_a^1(0)$ to alter the activity level in the model. An analysis of whether this yields physiologically reasonable transducer currents is presented in Sec. IV D.

IV. RESULTS

The finite element model is solved for unit stapes displacement input which represents the acoustic input. A mesh discretization of 1041 nodes along x direction and 41 nodes along z direction was used for the model. The convergence and sensitivity to the discretization are discussed in Ref. 20. All results presented in this section are with respect to the stapes input and use three symmetric fluid modes and a feedforward distance of 5 μm. To alter the activity level we change the maximum MET channel sensitivity ($G_a^1(0)$) while leaving *all* other parameters constant. It is arguable whether reducing the MET sensitivity is equivalent to reduction in activity level. The other parameter controlling activity, ϵ_3, is not expected to change significantly over the small variation in transmembrane potential (<15 mV, see Ref. 2) seen *in vivo*. At higher acoustic levels the HB conductance would start saturating much earlier than ϵ_3 (if it does saturate at all). Therefore we approximate the higher sound input level by a lower MET sensitivity in the model. Naturally this is not strictly correct as we are ignoring nonlinearities in this model. In the results presented, $G_a^1(0) = 0$ S/m^2 represents a passive case while $G_a^1(0) = 4.19 \times 10^6$ S/m^2 represents the fully active case [see Sec. III B and Eq. (36)]. The following shows the model's response predictions to acoustic input at varying locations, varying activity levels, response to impulse input, frequency glides exhibited by the model, and the BM motion relative to the ST potential (magnitude and phase). We start with the frequency response of the model at different locations along the BM.

A. Frequency response

1. Different locations along the BM

Figures 5 and 6 show magnitude and phase, respectively, of the BM frequency response referenced to stapes motion at different locations for high activity and no activity (passive model). The model exhibits familiar tuning curves from base to apex. The response shifts to lower frequencies by about half an octave when activity is lowered and amplitude drops by about 35 dB from active to passive for basal locations.

2. Different activity levels

Figures 7 and 8 show magnitude and phase, respectively, at $x=6$ mm for different activity levels overlapped with experimental results from Cooper [Fig. 1(a) in Ref. 39]. Figures 9 and 10 show the same model results overlapped with experimental results from deBoer and Nuttall.[40] In the magnitude plots, the BM gain with respect to stapes is normalized to the maximum passive/dead response. At frequencies lower than the best frequency, the model response (either phase or amplitude) is insensitive to alterations in the level of activity, consistent with experimental observations. The

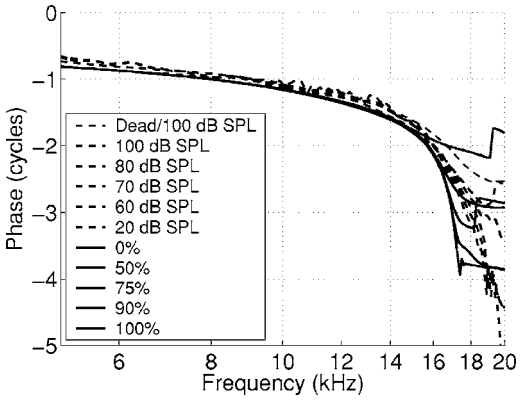

FIG. 10. Dash lines: Guinea pig data from deBoer (Ref. 40) (data supplied by E. deBoer). Thick lines: BM phase in cycles (2π rad) at 6 mm for different levels of activity [100% activity is equivalent to a conductance slope of $G_a^1(0)=4.19\times10^6$ S/m^2].

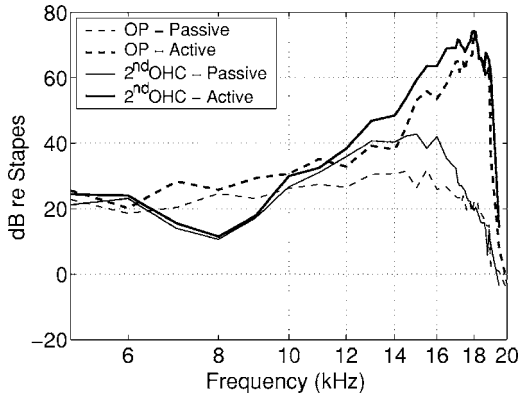

FIG. 11. Experimental results for the guinea pig BM gain envelope at the outer pillar (OP) location and the second (middle) row OHC location from Ref. 41. The thick lines represent the active response while thin lines represent the passive response. Notice that the maximum passive response depends on the radial location where it is measured.

close match between the model prediction and the experimental data for the frequency dependence of the BM gain is evident in Figs. 7 and 9. In comparing the two magnitude plots (Figs. 7 and 9), the variability in the experimental data should be noted. For example, the relative gain from 100 to 70 dB SPL is around 11 dB for data from Cooper[39] while the relative gain is around 17 dB for data from deBoer and Nuttall.[40] The model predicts a relative gain of approximately 35 dB from the passive state [represented by $G_a^1(0)=0$ in the model] to the state with maximum activity. A similar relative gain is also seen in experiments as we transition from high intensity acoustic input (where the effect of active force generation in the cochlea is expected to be minor) to low intensity acoustic input (where the cochlea is at its most sensitive). The characteristic frequency (CF) of the location also shifts by around half an octave in both the model and the experiments with the reduction in activity, which is embodied by a lower MET sensitivity in the model and increased acoustic sound input level in the experiments. The phase comparisons in Figs. 8 and 10 too show a close match between the experiments and the model, although the passive response of the model does not accumulate as much phase lag as is seen in experiments at high sound levels.

Magnitude predictions of the model are sharper than the experimental values (i.e., Q_{10} dB for the model is higher than the experiment). The sharpness of response varies among experiments and does depend on processing of the data somewhat (as is evident from Figs. 7 and 9). Even including such experiment-to-experiment variability, the model exhibits a higher Q_{10} factor than seen in a typical experiment. This sharp response also results in a longer impulse response as shown in Sec. III B. We speculate that the main reason for this discrepancy is the lack of longitudinal structural coupling along the BM and the TM in the model. Although we have not directly compared absolute gains, our model predicts the passive response [$G_a^1(0)=0$ S/m^2] to be around 10 dB higher than both the results in Refs. 39 and 40. The passive gain of the model is around 33 dB (see Fig. 5). It should be noted that the magnitude observed in experiments depends on the location of the bead on the BM.[22] Passive gain as high as 40 dB has been measured in experiments (results reproduced in Fig. 11). Envelopes of guinea-pig BM response data from Ref. 41 for acoustic levels varying from 8 to 100 dB SPL at two different radial locations are shown in Fig. 11 to demonstrate the spatial variability of the BM response. As Fig. 11 shows, the measured passive gain of the BM is as high as 40 dB when measured near the middle OHC location but is only 30 dB when measured at an outer pillar location.

B. Impulse response

The impulse response of the model was obtained by first simulating the model at different frequencies (100 Hz to 20 kHz in 100 Hz steps) and then applying the inverse Fourier transform at a given location. Figure 12 shows the impulse response of the model for an active and a passive case

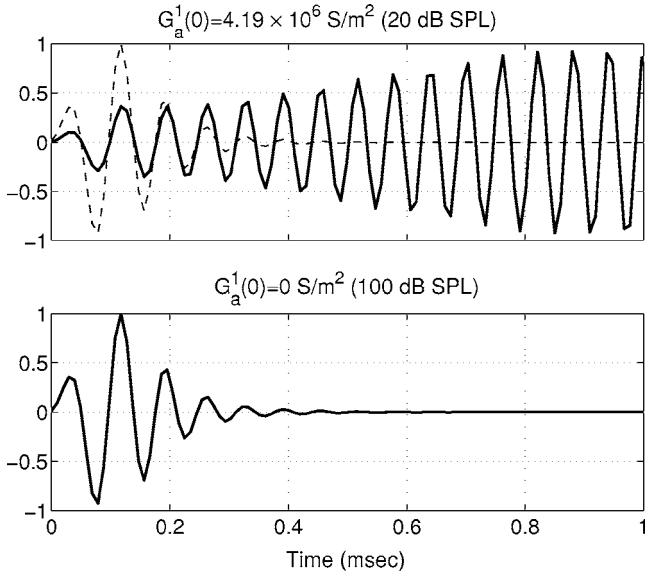

FIG. 12. Normalized model predictions of the BM impulse response at 6 mm for a highly active and a passive case. Active case corresponds roughly to gain seen at 20 dB SPL, while passive case corresponds to gain seen at 100 dB SPL or in a dead cochlea. The thin dashed line in the top panel is the 100 dB SPL result superimposed to highlight the near invariance of the zero crossings of the response.

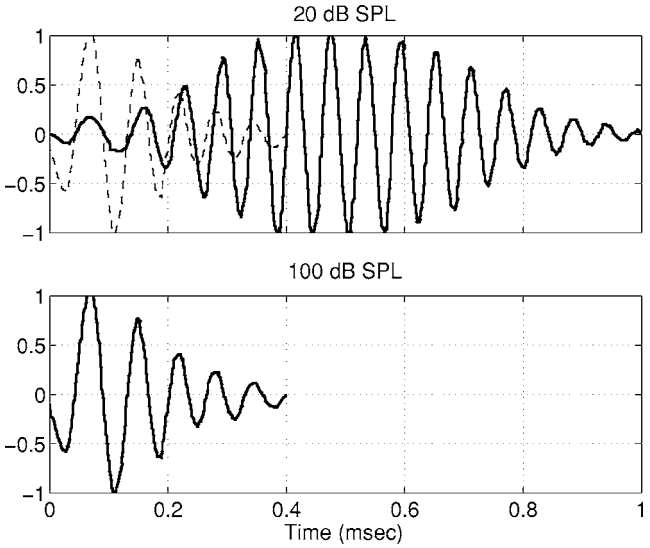

FIG. 13. Normalized experimental BM impulse response as shown in Ref. 40. Acoustic levels for the two plots are 20 and 100 dB SPL (dead cochlea). The thin dashed line in the top panel is the 100 dB SPL result superimposed to highlight the near invariance of the zero crossings of the response.

(roughly corresponding to a 20 and a 100 dB SPL case as per Fig. 9) and Fig. 13 shows the experimentally derived impulse response as seen by Ref. 40 in a guinea pig. The passive response of the model compares well with the experiment but the active response shows oscillations that continue on up to 3 ms (the figure shows response only up to 1 ms to aid comparison between model and experiment). This would be expected as the model has a sharper frequency response than the experimental data. As in the experimental data (e.g., Ref. 40 and in the theoretical study by Ref. 42), the model also shows the same zero crossings of the response for the initial few cycles (indicated by the passive response superimposed as thin dashed line over the active response). The model does not exhibit any ringing behavior often seen in experimental data[43] and also reproduced by nonlinear models.[26] This suggests that ringing could be primarily due to nonlinear effects in the cochlea.

Figure 14 shows the frequency glide for the active impulse response shown in Fig. 12. The glide represents the instantaneous frequency at a given time of the impulse response. The instantaneous frequency is much lower than the CF of the location at the start of the impulse response but grows rapidly to reach the CF. This result is very similar to the glides observed experimentally (e.g., Refs. 43 and 44).

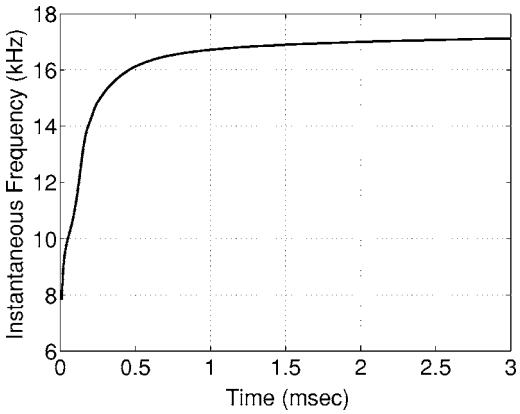

FIG. 14. Frequency glide at 6 mm for the most active case ($G_a^1(0)=4.19\times10^6$ S/m^2) which roughly corresponds to a 20 dB SPL acoustic input as per Fig. 9 for the 17 kHz CF location.

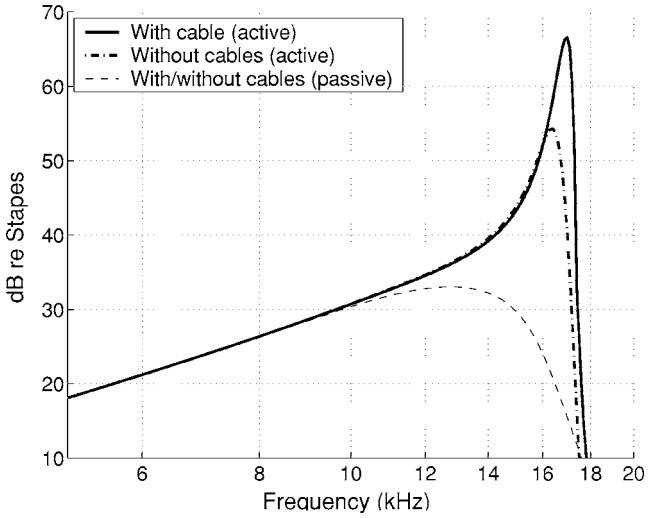

FIG. 15. BM response magnitude at 6 mm in decibels with respect to stapes motion for active [thick lines, $G_a^1(0)=4.19\times10^6$ S/m^2] and passive case [thin line, $G_a^1(0)=0$ S/m^2], with and without longitudinal cables. The passive curves virtually overlap and so only one of them is plotted.

C. Removal of cables

One interesting test that can be done using the model is to evaluate the importance of current conduction along the length of the cochlea to the BM amplification. To run this test we disabled the longitudinal cables and solved for the system response to acoustic input.

Figure 15 shows the absence of the cables has a measurable impact on cochlear amplification when activity is high. The effect is negligible when the model is passive. There is a loss in amplification of around 10 to 15 dB when cables are removed. The model results imply that current conduction along the length of the cochlea also plays a role in active amplification in the cochlea.

D. Potentials and currents

We have shown so far that the mechanical response of the BM compares favorably with experimental results. The validity of the model results depends on whether the voltages in the different scalae and the currents predicted by the model are within certain reasonable limits. Voltages or currents too large or too small compared to experimentally measured quantities would indicate possible shortcomings of the model. This model has been constructed with an aim to test efficacy of OHC forcing at high frequencies. The model produces high amplification at the base like in experiments using only active somatic forcing from OHCs. We therefore report the model predictions at a basal location and compare those currents and voltages with experimental values. Since the model is linear, the model predictions should be compared with very low level acoustic data. We use a BM displacement of 0.5 nm as a reference for stating the voltages

and currents assuming that the cochlear response shows a linear input-output relation up to around 0.5 nm BM displacement (see Fig. 3 in Ref. 45). At the 17 kHz best place, data from Ref. 41 suggest that a 10 dB SPL acoustic input will give a 0.5 nm BM response while that from Ref. 39 suggest that a 30 dB SPL acoustic input is needed to achieve the same. A 0.5 nm displacement of the BM is therefore considered to roughly correspond to a 20 dB SPL sound input.

With the highest value of MET sensitivity [$G_a^1(0) = 4.19 \times 10^6$ S/m^2, or at $x=6$ mm, $G_a^1(0.6) = 0.91 \times 10^6$ S/m^2] the model predicts a transducer current of 1.56 nA and a transmembrane potential of 0.62 mV for 0.5 nm BM displacement at the 17 kHz best place ($x=6$ mm). Corresponding predicted maximum displacements for HBs and OHCs at $x=6$ mm are 2.5 and 3.5 nm respectively, per nm of BM displacement. The maximum predicted active force from one OHC on the BM at $x=6$ mm is 0.12 nN/nm of BM displacement. Recent estimates for transducer currents in gerbils are available in Ref. 12. The maximum current measured by He *et al.*[12] at a basal location in a hemicochlea preparation was around 2.5 nA. According to corrections presented in Ref. 13 for reduced endocochlear potential, reduced body temperature of the animal, and differences in endolymphatic cations, the current *in vivo* is expected to be around four times higher than what was observed in Ref. 12. This gives us an estimate of 10 nA for the maximum transducer current. A review by Robles *et al.*[45] indicates that typically transduction channels are saturated at 100 dB SPL sound input (as inferred from the linear growth in BM response beyond 100 dB SPL). Guinea pig data from Refs. 41 and 39 suggest that at 100 dB SPL acoustic input, the BM displacement is less than 20 nm. Making a linear approximation of the transducer current to BM displacement relation yields a sensitivity of 0.5 nA/nm of BM displacement. This is an extremely conservative estimate since the MET sensitivity is expected to be highest (or close to its highest value) near the resting state and greatly reduced as the channels saturate.[9] The transducer current sensitivity therefore is likely to be much higher than 0.5 nA/nm. This model for the most sensitive case at the 6 mm site (the 17 kHz best place), predicts a transducer current of 3.12 nA/nm of BM displacement, which is around six times higher than the 0.5 nA/nm lower bound estimated earlier. To summarize, for the most sensitive model, our predictions of HB currents (1.56 nA at ≈20 dB SPL) are lower than the maximum values given in the literature.

The ST voltage

In an interesting experiment, Fridberger *et al.*[46] measured OoC potentials in response to acoustic stimulation. They observed that ST voltage and BM velocity profiles are very similar in acoustic stimulation and the phase difference between ST and BM has a sharp increase near the best place. We compare our model predictions of the ST voltage with the experimental data of Fridberger *et al.* (2004). The location chosen is $x=5.85$ mm, which has a CF of 17.4 kHz, the same as the CF of the location in the experiment of Ref. 46.

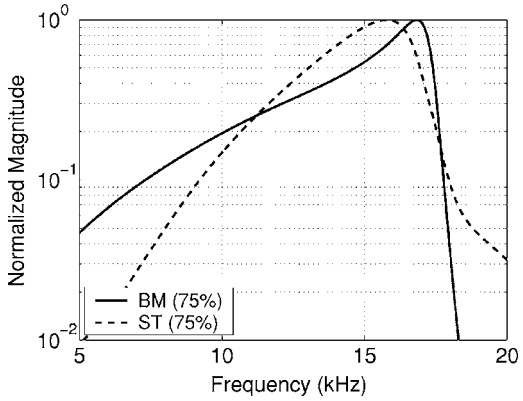

FIG. 16. Model prediction of the magnitudes of the BM displacement and ST voltage at 75% activity [$G_a^1(0) = 3.14 \times 10^6$ S/m^2] normalized to their respective maximum levels, plotted vs frequency of the acoustic stimulus. Location is $x=5.85$ mm (CF≈17.4 kHz).

Experimental results from Ref. 46 show that the BM displacement and OoC voltage have nearly the same frequency dependence when normalized to their maximum response at the CF (experimental results for magnitude not reproduced here). For the most active case [i.e., when the MET sensitivity is maximum $G_a^1(0) = 4.19 \times 10^6$ S/m^2], our model predicts that the BM displacement is much more sharply tuned than the ST voltage. When a lower level of activity (as embodied by a lower MET sensitivity) is used the normalized profiles of ST voltage and BM displacement match each other more closely as in the experiments (see model prediction for 75% activity shown in Fig. 16). In terms of absolute magnitude, the model predicts 0.17 mV for 1 nm of BM displacement (0.24 mV rms) for the lower MET sensitivity [$G_a^1(0) = 3.14 \times 10^6$ S/m^2, or 75% activity], while Ref. 46 shows around 0.15 mV rms ST potential when BM displacement is 1 nm at 40 dB SPL. Model results for the phase difference between BM displacement and ST voltage (Fig. 17) are in good agreement with experimental measurements from Ref. 46. The phase difference is nearly constant until near the CF where it jumps over 300° for the most

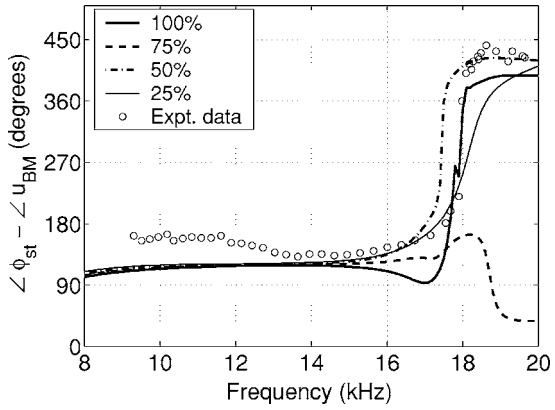

FIG. 17. Phase difference between BM displacement and ST voltage plotted vs frequency of acoustic stimulus for different activity levels [100% activity is equivalent to a conductance slope of $G_a^1(0) = 4.19 \times 10^6$ S/m^2]. Location is $x=5.85$ mm (CF≈17.4 kHz both in experiment and model). Experimental data from Ref. 46.

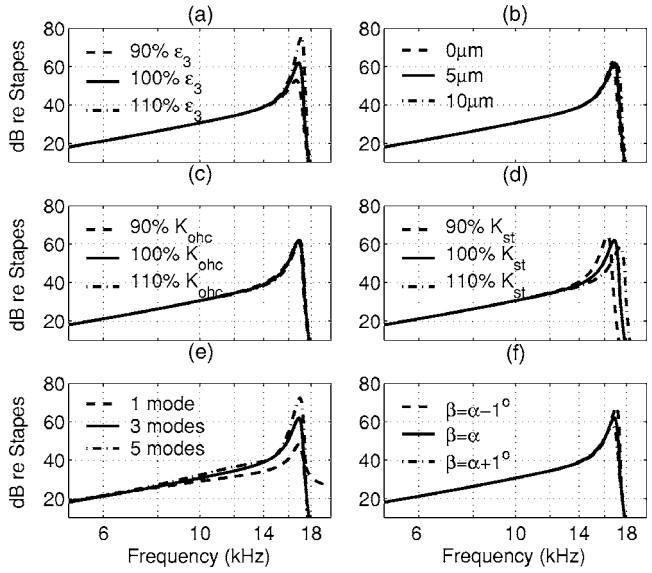

FIG. 18. Gain of the BM displacement compared for different: (a) OHC electromechanical coupling coefficient (ϵ_3), (b) feed-forward distance, (c) OHC stiffness (K_{ohc}), (d) HB stiffness (K_{hb}), (e) number of fluid modes, and (f) HB angle (angle β, see Fig. 3). Location is $x=6$ mm (CF$\approx$17 kHz), $G_a^1(0)=3.98\times10^6$ S/m^2 or 95% active.

active case. As was observed by Ref. 46, the jump does not increase in a monotonic manner with increasing acoustic level.

The results from Ref. 46 were suggested to be in support of a theory on OHC somatic motility proposed by Dallos and Evans.[36] The Dallos–Evans theory is that OHC somatic motility is driven not by fluctuations in the transmembrane voltage, but by fluctuations in the extracellular voltage. Our model has OHC somatic motility driven by fluctuations in the transmembrane voltage and yet the model predicts results similar to those seen in Ref. 46. The use of data from Ref. 46 in favor of the Dallos–Evans theory is therefore questionable.

V. PARAMETER SENSITIVITY

In the following, we investigate the effect of varying a few of the key parameters in the model that are expected to influence the BM motion significantly. The sensitivity of the model to the MET conductance is evident from the results presented in the preceding results section. In Fig. 18 we show the change in the model response when small changes are made in HB stiffness (K_{hb}), OHC stiffness (K_{ohc}), OHC electromechanical coupling coefficient (ϵ_3), HB orientation in the cochlea (angle β), number of fluid modes, and the feed-forward distance. The conductance slope was set at 95% of the maximum value for all plots in Fig. 18 ($G_a^1(0)=3.98\times10^6$ S/m^2) to avoid the model transitioning into an unstable region.

A. Electromechanical coupling

The model exhibits higher cochlear amplification for a higher electromechanical coupling coefficient [Fig. 18(a)]. The model response is sensitive to this parameter with over 5 dB change in BM gain when the electromechanical coupling parameter is changed by 10%. A higher electromechanical coupling coefficient implies higher force generation by OHCs so this result is expected.

B. Feed-forward distance

Unlike the model developed by Lim and Steele,[26] this model is not highly sensitive to the forward inclination angle of the OHCs [Fig. 18(b)]. Lim and Steele[26] proposed that the forward inclination of OHCs plays a significant role in cochlear tuning and amplification. They use a gain factor to account for the feed-forward effect. In this model, the effect of the forward inclination of OHCs is negligible. Nonetheless we cannot rule out the possibility that if the pressure forcing on the TM is accurately modeled, it might show that effect of feed-forward is larger than what is seen here. Furthermore, a different selection of parameters (values and functional dependence) and the inclusion of longitudinal structural coupling may influence this conclusion.

C. OHC stiffness

Changing OHC stiffness by 10% has a very small effect on the BM response [Fig. 18(c)]. Increased OHC stiffness gives a higher gain in the BM response with respect to the stapes while a lower OHC stiffness yields a smaller BM response (not discernible in the figure). This is consistent with the implication in Ref. 4 that increased OHC stiffness leads to higher cochlear amplification. This result should be interpreted with caution though. It is likely that other factors (such as the OHC basolateral capacitance and electromechanical coupling coefficient) were also affected in Ref. 4 along with the OHC stiffness when the current was injected in the cochlea, so a direct comparison is not possible unless all affected parameters in the experiment can be identified.

D. HB stiffness

A change in the HB stiffness causes a shift in the characteristic frequency of the location [Fig. 18(d)]. In the model the HB stiffness dominates stiffness loading on the TM due to which the resonance mode of the OoC shifts when this stiffness is altered. This points to a more prominent role for HBs if HB motility is present.

E. Fluid modes

For the box model of the cochlea, increasing the number of fluid modes represents the transition from a two-dimensional cochlear model (one mode) to a three-dimensional model (more than one mode). However, since the shape of the cross section in the cochlea is unlike a rectangular box, the results shown here should only be taken as indicative of the behavior possible in a cochlear model with a more realistic geometry. Figure 18(e) shows the model prediction for magnitude of the BM response with 95% activity [i.e., $G_a^1(0)=3.98\times10^6$ S/m^2] at $x=6$ mm with five, three, and one fluid mode. As the results show, having more fluid modes influences the rate of amplitude drop after the best place and also improves active amplification in the model. The passive cut-off behavior also improves (not shown)

when higher modes are used and the passive curves shift to more lower frequencies. However, the passive gain is largely unaffected by the number of fluid modes.

F. HB angle

To study the role played by the kinematic configuration used in the model one can simulate the model with small perturbations to the different angles and lengths of the structures. The most critical kinematic feature of them is the relative angle between the HBs and the OHCs. Figure 18(f) shows BM response when HB angles (β) are changed slightly keeping the OHC angles (α) the same. A very small change was used since the model is at high activity [$G_a^1(0) = 3.98 \times 10^6$ S/m^2] and can be easily made unstable if large changes in angle are used. If the HB angle is smaller than OHC angle, the model predicts a higher BM gain. If one looks at the deformation statically, the upward motion of the BM would result in larger rotation of the HBs in the excitatory direction and therefore would result in more transducer current and more OHC forcing if the HB angle is smaller than OHC angle. Having all the HBs "leaned back" in the direction of the tallest HB would thus give better BM amplification.

VI. CONCLUSION

The main purpose of the present paper was to describe and vet a mathematical model of the cochlea. In this paper, we have presented a physiologically motivated mechanical-electrical-fluidic model for predicting the response of the cochlea to acoustical stimulus. The model explicitly couples the mechanical and electrical degrees of freedom through a piezoelectric model of OHC electromotility and includes the conduction of electrical energy down the length of the cochlea. HB motility is not included in this model. We have shown that by changing a single parameter, the MET sensitivity, the model captures a wide range of experimentally observed effects in the cochlea. The model predictions of the transducer currents, receptor potentials, and mechanical response (BM displacement) compare closely to available experimental data. Under a variation of the model parameters, we have shown that the qualitative nature of the predictions do not change dramatically, although the details of the response certainly do. We do not claim that the model gives a complete picture of cochlea. Key simplifications include the linearization of all response variables about their operating points, and the simplification of the fluid geometry. We do claim to have made progress on describing how electromotile processes might work in the cochlea, especially in the basal portion. The model brings to light the following two important points in cochlear mechanics:

1. Modes of vibration of the OoC: What is thought of as the resonance of the BM should be interpreted as the local resonance of the OoC system. Our simplified kinematical approximation to the OoC system suggests, as does experimental work,[32] that structures of the OoC other than the BM, especially the TM, play a prominent role in the cochlea. Observations of a notch in the BM frequency response to bipolar stimulation[8] are indicative of a resonance in the OoC and give further credence to this assertion.
2. Intimate link between the electrical currents/voltages and OoC micromechanics: The elements in the OoC together with the electrical environment form a complex feedback system. To accurately model the feedback force arising from the OHCs or HBs it is essential to have all the individual elements modeled in the system. In addition to providing for a predictive model, the availability of current and voltage responses provide additional data to verify the validity of the model.

It is emphasized here that the highest RC-cutoff frequency is around a 1000 Hz for the basal cells in the model. The model predictions for the forces generated by OHCs, the receptor potential, the OoC potential (equivalent to the ST potential in our model), and the transducer currents all fall below maximum measured values. Hence the model developed herein shows how an electromechanical system can interact to overcome filtering of the transmembrane potential by the membrane capacitance. The MET sensitivity (probably most reliably quantified experimentally *in situ* by the BM displacement to transducer current measurement as HB motion is difficult to measure in that setting) used in the model is likely higher than the sensitivity *in vivo*. As the results in Sec. V indicate, the model response is sensitive to parameters and a perhaps further optimization of the parameters could lead to a lower estimate of the maximum MET sensitivity. We conjecture here that it is quite possible that a higher MET sensitivity is needed in the present model to overcome the lack of HB motility in the model. The HBs are of course ideally situated to aide in channel opening and thereby affecting the conductance of the channels. Further experimental and theoretical work is needed to validate such a hypothesis. It is therefore claimed that HB forcing, if present, acts in conjunction with the OHC somatic forcing to give rise to cochlear amplification as suggested in a recent finding by Kennedy *et al.*[47]

ACKNOWLEDGMENTS

The authors would like to thank Nigel Cooper, Egbert deBoer, and Alfred Nuttall for supplying the experimental data that were used for comparisons with the model predictions and for their helpful insights in interpreting the data. This work was supported by National Institutes of Health Grant No. NIDCD R01-04084.

[1] G. V. Bekesy, *Experiments in Hearing* (McGraw Hill, New York, 1960).
[2] P. Dallos, J. Santos-Sacchi, and A. Flock, "Intracellular recordings from cochlear outer hair-cells," Science **218**, 582–584 (1982).
[3] A. Hubbard and D. C. Mountain, "Alternating current delivered into the scala media alters sound pressure at the eardrum," Science **222**, 510–512 (1983).
[4] A. A. Parthasarathi, K. Grosh, J. F. Zheng, and A. L. Nuttall, "Effect of current stimulus on in vivo cochlear mechanics," J. Acoust. Soc. Am. **113**, 442–452 (2003).
[5] W. E. Brownell, C. R. Bader, D. Bertrand, and Y. D. Ribaupierre, "Evoked mechanical responses of isolated cochlear hair cells," Science **227**, 194–196 (1985).
[6] J. F. Zheng, T. Y. Ren, A. Parthasarathi, and A. L. Nuttall, "Quinine-

induced alterations of electrically evoked otoacoustic emissions and cochlear potentials in guinea pigs," Hear. Res. **154**, 124–134 (2001).
[7]G. Frank, W. Hemmert, and A. W. Gummer, "Limiting dynamics of high-frequency electromechanical transduction of outer hair cell," Proc. Natl. Acad. Sci. U.S.A. **96**, 4420–4425 (1999).
[8]K. Grosh, J. F. Zheng, Y. Zou, E. de Boer, and A. L. Nuttall, "High-frequency electromotile responses in the cochlea," J. Acoust. Soc. Am. **115**, 2178–2184 (2004).
[9]P. Dallos, "Overview: Cochlear neurobiology," in *The Cochlea*, edited by P. Dallos, A. N. Popper, and R. R. Fay (Springer, New York, 1996).
[10]P. Martin, D. Bozovic, Y. Choe, and A. J. Hudspeth, "Spontaneous oscillation by hair bundles of the bullfrog's sacculus," J. Neurosci. **23**, 4533–4548 (2003).
[11]H. J. Kennedy, A. C. Crawford, and R. Fettiplace, "Force generation by mammalian hair bundles supports a role in cochlear amplification," Nature (London) **433**, 880–883 (2005).
[12]D. Z. Z. He, S. P. Jia, and P. Dallos, "Mechanoelectrical transduction of adult outer hair cells studied in a gerbil hemicochlea," Nature (London) **429**, 766–770 (2004).
[13]H. J. Kennedy, M. G. Evans, A. C. Crawford, and R. Fettiplace, "Fast adaptation of mechanoelectrical transducer channels in mammalian cochlear hair cells," Nat. Neurosci. **6**, 832–836 (2003).
[14]S. Neely, "A model of cochlear mechanics with outer hair cells motility," J. Acoust. Soc. Am. **94**, 137–146 (1993).
[15]C. D. Geisler and C. Sang, "A cochlear model using feed-forward outer-hair cells forces," Hear. Res. **86**, 132–146 (1995).
[16]P. J. Kolston, "Comparing in vitro, in situ, and in vivo experimental data in a three-dimensional model of mammalian cochlear mechanics," Proc. Natl. Acad. Sci. U.S.A. **96**, 3676–3681 (1999).
[17]K. M. Lim and C. R. Steele, "A three-dimensional nonlinear active cochlear model analyzed by the wkb-numeric method," Hear. Res. **170**, 190–205 (2002).
[18]R. S. Chadwick, E. K. Dimitriadis, and K. H. Iwasa, "Active control of waves in a cochlear model with subpartitions," Proc. Natl. Acad. Sci. U.S.A. **93**, 2564–2569 (1996).
[19]E. K. Dimitriadis and R. S. Chadwick, "Solution of the inverse problem for a linear cochlear model: A tonotopic cochlear amplifier," J. Acoust. Soc. Am. **106**, 1880–1892 (1999).
[20]A. A. Parthasarathi, K. Grosh, and A. L. Nuttall, "Three-dimensional numerical modeling for global cochlear dynamics," J. Acoust. Soc. Am. **107**, 474–485 (2000).
[21]R. C. Naidu and D. C. Mountain, "Measurements of the stiffness map challenge a basic tenet of cochlear theories," Hear. Res. **124**, 124–131 (1998).
[22]M. Homer, A. Champneys, G. Hunt, and N. P. Cooper, "Mathematical modeling of the radial profile of basilar membrane vibrations in the inner ear," J. Acoust. Soc. Am. **116**, 1025–1034 (2004).
[23]W. Rall, "Core conductor theory and cable properties of neurons," in *Handbook of Physiology: The Nervous System*, edited by E. R. Kandel, J. M. Brookhardt, and V. B. Mountcastle (Williams and Wilkins, 1997), Vol. **1**, Chap. 3, pp. 39–98.
[24]P. Dallos, "Organ of corti kinematics," J. Assoc. Res. Otolaryngol. **4**, 416–421 (2003).
[25]N. V. Deo and K. Grosh, "Simplified nonlinear outer hair cell models," J. Acoust. Soc. Am. **117**, 2141–2146 (2005).
[26]K. M. Lim and C. R. Steele, "Response suppression and transient behavior in a nonlinear active cochlear model with feed-forward," Int. J. Solids Struct. **40**, 5097–5107 (2003).
[27]A. W. Gummer, B. M. Johnstone, and N. J. Armstrong, "Direct measurement of basilar membrane stiffness in guinea pig," J. Acoust. Soc. Am. **70**, 1298–1309 (1981).
[28]C. Fernandez, "Dimensions of the cochlea (guinea pig)," J. Acoust. Soc. Am. **24**, 519–523 (1952).
[29]D. Strelioff and A. Flock, "Stiffness of sensory-cell hair bundles in the isolated guinea-pig cochleas," Hear. Res. **15**, 19–28 (1984).
[30]D. Z. Z. He and P. Dallos, "Properties of voltage-dependent somatic stiffness of cochlear outer hair cells," J. Assoc. Res. Otolaryngol. **1**, 64–81 (2000).
[31]J. J. Zwislocki and L. K. Cefaratti, "Tectorial membrane. II Stiffness measurement in vivo," Hear. Res. **42**, 211–228 (1989).
[32]A. W. Gummer, W. Hemmert, and H. P. Zenner, "Resonant tectorial membrane motion in the inner ear: Its crucial role in frequency tunings," Proc. Natl. Acad. Sci. U.S.A. **93**, 8727–8732 (1996).
[33]K. E. Nilsen and I. J. Russell, "The spatial and temporal representation of a tone on the guinea pig basilar membrane," Proc. Natl. Acad. Sci. U.S.A. **97**, 11751–11758 (2000).
[34]A. A. Spector, W. E. Brownell, and A. S. Popel, "Effect of outer hair cell piezoelectricity on high-frequency receptor potentials," J. Acoust. Soc. Am. **113**, 453–461 (2003).
[35]G. D. Housley and J. F. Ashmore, "Ionic currents of outer hair-cells isolated from the guinea-pig cochlea," J. Physiol. (London) **448**, 73–98 (1992).
[36]P. Dallos and B. N. Evans, "High-frequency motility of outer hair cells and the cochlear amplifier," Science **267**, 2006–2009 (1995).
[37]D. Strelioff, "Computer-simulation of generation and distribution of cochlear potentials," J. Acoust. Soc. Am. **54**, 620–629 (1973).
[38]K. H. Iwasa and M. Adachi, "Force generation in the outer hair cell of the cochlea," Biophys. J. **73**, 546–555 (1997).
[39]N. P. Cooper, "Harmonic distortion on the basilar membrane in the basal turn of the guinea-pig cochlea," J. Physiol. (London) **509**, 277–288 (1998).
[40]E. de Boer and A. L. Nuttall, "The mechanical waveform of the basilar membrane. III. Intensity effects," J. Acoust. Soc. Am. **107**, 1497–1507 (2000).
[41]A. L. Nuttall and D. Dolan, "Steady-state sinusoidal velocity responses of the basilar membrane in guinea pig," J. Acoust. Soc. Am. **99**, 1556–1565 (1996).
[42]C. A. Shera, "Intensity-invariance of fine time structure in basilar-membrane click responses: Implications for cochlear mechanics," J. Acoust. Soc. Am. **110**, 332–348 (2001).
[43]A. Recio, N. C. Rich, S. S. Narayan, and M. Ruggero, "Basilar-membrane responses to clicks at the base of the chinchilla cochlea," J. Acoust. Soc. Am. **103**, 1972–1989 (1998).
[44]E. de Boer and A. L. Nuttall, "The mechanical waveform of the basilar membrane. I. Frequency modulations (glides) in impulse responses and cross-correlation functions," J. Acoust. Soc. Am. **101**, 3583–3592 (1997).
[45]L. Robles and M. A. Ruggero, "Mechanics of the mammalian cochlea," Physiol. Rev. **81**, 1305–1352 (2001).
[46]A. Fridberger, J. B. de Monvel, J. Zheng, N. Hu, Y. Zou, T. Ren, and A. Nuttall, "Organ of corti potentials and the motion of the basilar membrane," J. Neurosci. **24**, 10057–10063 (2004).
[47]H. J. Kennedy, M. G. Evans, A. C. Crawford, and R. Fettiplace, "Depolarization of cochlear outer hair cells evokes active hair bundle motion by two mechanisms," J. Neurosci. **26**, 2757–2766 (2006).